Research papers

Reactivation of dissolved polysulfides with nitrogen doped graphene decorated carbon cloth as an effective interlayer for magnesium-sulfur battery

Dasari Bosubabu [a,b,*], Mohsen Sotoudeh [a,c], Liping Wang [d], Zhenyou Li [a,b], Thomas Diemant [a], Guruprakash Karkera [a,b], Ebrahim Abouzari-Lotf [a,b], Axel Groß [a,c], Maximilian Fichtner [a,b], Zhirong Zhao-Karger [a,b]

[a] Helmholtz Institute Ulm (HIU) Electrochemical Energy Storage, Helmholtzstraße 11, Ulm D-89081, Germany
[b] Institute of Nanotechnology, Karlsruhe Institute of Technology (KIT), Hermann-von-Helmholtz-Platz 1, Eggenstein-Leopoldshafen D-76344, Germany
[c] Institute of Theoretical Chemistry, Ulm University, Albert-Einstein-Allee 11, 89081 Ulm, Germany
[d] Institute for Organic Chemistry II and Advanced Materials, Ulm University, Albert-Einstein-Allee 11, Ulm 89081, Germany

ARTICLE INFO

ABSTRACT

The theoretically high energy densities and wide availability of active materials have led to great interest in the development of magnesium-sulfur (Mg—S) batteries. However, poor electronic conductivity of sulfur, active material dissolution, polysulfide shuttling, and poor cycling stability are major challenges that need to be tackled. Herein we observed the pristine Mg—S cell faces significant overcharging issues and cell failure is common within 30 cycles with significant capacity decay. With the help of XRD and elemental mapping realized that the dissolved liquid polysulfides are metastable in nature. Due to the high sulfophilic nature of the separator, polysulfide absorption leads to slow crystal growth inside the separator. This active material trapping might be the reason for quick capacity decay. We attempted to revive the dissolved polysulfides by introducing conductive nitrogen-doped graphene (N-gpn)@Carbon cloth(CC) interlayer between the electrodes and separator. This interlayer has a high polysulfide absorption nature, which allows the battery to demonstrate an initial capacity of 1075 mAh g^{-1} and increased cycling stability to 100 cycles. However, this stability was further enhanced to 300 cycles by protecting the anode. Theoretical considerations suggest that among all polysulfides, MgS$_8$, has the strongest interaction with N-gpn and can be trapped most favorably in a defective N-gpn. This leads to enhanced utilization of the active material and improved cycling stability.

1. Introduction

The steadily increasing demand for efficient, clean energy storage technology brings lithium-ion batteries forefront of the global market, owing to the high energy density, long cycle life, and lightweight lithium (Li). [1,2] However, considering its practical energy density limitations, safety issues, and limited natural resources for the electrode materials of present Li-ion batteries, researchers are motivated to investigate alternative battery technologies based on sustainable materials. In this view, magnesium-sulfur (Mg—S) battery chemistry is promising due to the high theoretical energy density (1722 Wh kg^{-1} and 3200 Wh L^{-1}), high availability of raw materials, and potential cost-effectiveness [3–8].

Most importantly, it is believed that the low tendency of dendrite formation of Mg metal during stripping/platting provides better safety than Li metal batteries [9,10].

Though Mg—S batteries possess high theoretical energy density values, their practical achievements till now are limited due to the battery chemistry complications that might originate from the anode, cathode, and electrolyte of the cell. More importantly, the fundamental drawback of the sulfur cathode, such as its low electrical conductivity (5 × 10^{-30} S cm^{-1} at 25 °C) makes it difficult to accept electrons from the current collector, causing low active material utilization in the first discharge, this process continuously happening in the consecutive cycles [11–15]. Furthermore, during the reaction, the soluble magnesium

polysulfide in the ether electrolyte participates in the shuttle process [16–18]. This unavoidable polysulfide shuttle in ether-based electrolytes forms a passive layer on the anode by reducing itself, which consequences overcharging, low Coulombic efficiency, and fast capacity decay of the battery [19–21].

One of the effective approaches is using a conductive interlayer inserted between the cathode and separator. This interlayer acts as a filter to obstruct and trap the polysulfides and reactivate them [22,23]. In this scenario, due to its outstanding electrical, thermal, and mechanical properties, graphene has attracted considerable interest [24–26]. However, the weak interaction of nonpolar graphene with polar polysulfides displays low binding behavior, leading to the detachment of the reaction product (magnesium sulfides) from the electrode, which results in loss of electrical contact and capacity degradation [27,28]. Therefore, heteroatom (nitrogen, sulfur, phosphorus, oxygen, and boron) doping is introduced in the graphene matrix, which plays a significant role in enhancing polysulfide capture and improving cell performance in Li—S batteries [29–32]. Specifically, nitrogen doping has a distinct impact because it offers more active sites for ion absorption and improves electrochemical activity in addition to enhancing the electronic conductivity and wettability of the carbon. Hence, N-gpn shows tremendous importance in sulfur batteries.

In this work, we explore the critical role of protecting electrodes from polysulfide attack in Mg—S batteries. We introduce a novel N-gpn interlayer positioned between the cathode and separator. This interlayer tackles two key challenges: it enhances conductivity within the cathode for better sulfur utilization, and its nitrogen dopants effectively trap dissolved polysulfides, preventing them from reaching the anode. This dual functionality is evident in our findings. The N-gpn interlayer significantly extends cycling stability, from 30 to 100 cycles when placed near the cathode, and even further to 300 cycles near the anode. Additionally, the N-gpn may activate intermediate solid polysulfides, improving capacity retention. To further validate these results, we employed periodic density functional theory (DFT) calculations to understand the interaction between N-gpn and polysulfides.

In addition, we used conductive lithium polysulfide solution as a novel sulfur source in the cathode for the first time in the Mg—S battery. This conductive sulfur source along with the interlayer, resulting in a high initial capacity of 1075 mAh g^{-1} in the Mg—S battery. Unlike the traditional sulfur cathode prepared by the melt-diffusion method, this sulfur precipitation approach is way simple and accurate in case of material loading and allows uniform distribution of sulfur over the electrode.

2. Results and discussions

2.1. Structural analysis

The calculated density of states (DOS) of graphene, N-gpn, and the defective N-gpn (paired N-doped with carbon vacancy) with carbon vacancy derived from periodic DFT calculations are shown in Fig. 1a, along with their corresponding optimized structures. The filled valence band is predominantly of C-*p* character (green and blue) with some C-s orbitals (yellow) contribution. Carbon forms *sp*^{2}-hybrid orbitals are lying in the plane of the graphene sheet, with an angle of 120°. The bonding in-plane orbitals (green) are filled, and the antibonding orbitals are empty, explaining a honeycomb lattice of carbon atoms. The carbon *p*-orbitals oriented perpendicular to the graphene sheet (blue) are the states that dominate the band structure near the Fermi level. In the N-gpn, a carbon atom is substituted by a nitrogen atom, forming in the plane *sp*^{2}-hybrid orbitals with the carbon atoms. The perpendicular *p*-orbital of nitrogen contributes to the band structure near the Fermi level. In comparison to graphene, the Fermi level shifts upward by 1 eV, as shown in Fig. 1a. The defective N-gpn, paired N-gpn with carbon vacancy, shifts the Fermi level downward compared to the graphene, and the in-plane orbitals (green) contribute to the band structure close to the Fermi level (see Fig. 1a). Hence, the defective N-gpn might provide more reactive anchoring points to interact with the magnesium polysulfides
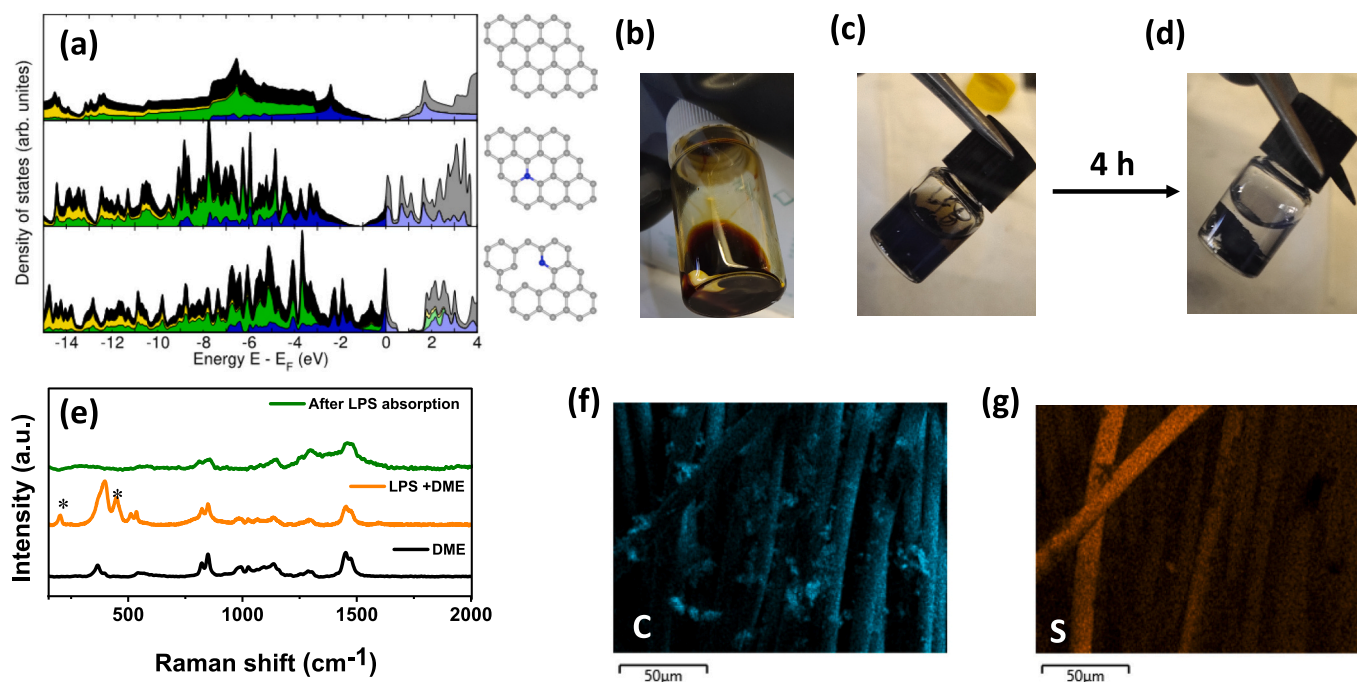

Fig. 1. Density of states (DOS) derived from DFT calculations of a graphene sheet, N-gpn, and the defective N-gpn (paired N-doped with carbon vacancy) from top to bottom, along with their corresponding optimized structures. The total DOS is given in black and gray. ~~Stacked~~ plotted on top of each other are the perpendicular *p*-orbitals (blue), the *p*-orbitals in the plane (green), and the *s*-projected density of states (yellow). Unoccupied states are drawn in a lighter color than the filled states. The energy zero is set to the top of the valence band. (b-c) Visual comparison of polysulfide adsorption test (e) Raman spectra of polysulfide solution before and after adsorption. (f, g) EDX elemental mapping of carbon and sulfur of N-gpn@CC after adsorption. (For interpretation of the references to color in this figure legend, the reader is referred to the web version of this article.)

than the pristine graphene sheet. In the experimental step, the structural properties of N-gpn were investigated by scanning electron microscopy (SEM) and the corresponding results are shown in Fig. S1. The 2D layered N-gpn particles have an average width of ~5 μm and are randomly distributed over the carbon cloth (CC) (Fig. S1a-c). A cross-sectional SEM image and corresponding elemental mapping results of N-gpn@CC are shown in Fig. S1d-f.

The polysulfide adsorption ability of the interlayer plays a vital role in the confinement of polysulfide. We tested this adsorption ability by adding N-gpn@CC to a lithium polysulfide (LPS) solution in DME. Fig. 1 (b-d) shows images of LPS, taken right after the addition of N-gpn@CC in LPS solution and after four hours; a clear decolorization becomes evident from the reference sample. To assess the degree of polysulfide adsorption, the LPS in DME solution was tested before and after N-gpn@CC absorption (after four hours of soaking) by Raman spectroscopy (Fig. 1e). For this purpose, the solution received after N-gpn@CC addition was transferred into a 0.7 mm glass tube and sealed with Teflon paste inside an Ar-filled glove box before starting the Raman measurement. The absence of polysulfide peaks below 500 cm^{-1} (cf. to the result of the pure LPS in the 200–500 cm^{-1} region [Fig. 1e]) indicates a complete removal of polysulfide from the solution (Fig. 1e), which confirms the strong polysulfide adsorption nature of the interlayer (both CC and N-gpn). Furthermore, elemental mapping was carried out on the vacuum-dried N-gpn@CC after polysulfide adsorption (Fig. 1f, g); the mapping confirms that the adsorbed polysulfides are uniformly distributed throughout the N-gpn@CC. Taken together, these test results demonstrate that the interlayer is highly efficient in absorbing polysulfides formed during the operation of a sulfur battery, and controls polysulfide shuttling (discussed later).

2.2. Electrochemical analysis

2.2.1. Discharge-charge stability analysis

Galvanostatic charge-discharge cycling experiments were performed with LPS@N-gpn cathode without and with an interlayer (N-gpn@CC) vs Mg/Mg^{2+} in a voltage window of 0.5–2.5 V at 0.1C. The LPS loading was maintained at 1 mg cm^{-2} by adding 0.1 M concentrated solution to each cathode. Interestingly, the LPS is oxidized to elemental sulfur in the Mg[B(hfip)$_4$]$_2$/DME electrolyte which is confirmed by Raman spectroscopy (Figs. S2–4). The charge-discharge profiles of without and with

interlayer cells are shown in Fig. 2. During the discharge process in both LPS@N-gpn (without interlayer) and N-gpn@CC (with interlayer) cells, two plateaus were observed at ~1.5 V and 1.1 V, representing the conversion of higher-order polysulfides to lower-order polysulfides (Fig. 2a,b). In contrast, the charging process showed only one plateau at ~2 V due to the conversion of solid magnesium sulfide to elemental sulfur through a polysulfide intermediate. [33] The interlayer cell initially showed a higher polarization (ΔE = 0.8 V), but decreased within 10 cycles to ΔE = 0.52 V and was also accompanied by an improvement in cell capacity. Interestingly, unlike in the LPS@N-gpn cell, an interlayer cell has a sloppy plateau below 1.1 V with high capacity (around 600 mAh g^{-1}) and this plateau was stable. This might indicates improving the reaction kinetics of lower-order polysulfides. Fig. 2c presents the cycling stability of cells with LPS@N-gpn and N-gpn@CC interlayer cathodes. The LPS@N-gpn cathode showed an initial discharge capacity of 638 mAh g^{-1} at 0.1C rate, after 30 cycles discharge capacity dropped to 293 mAh g^{-1} and the cell experienced the overcharging problem (this result is an average of 6 cells). The low capacity for this cell is most probably caused by self discharge of the cell (the high amount of polysulfide dissolution in the initial cycles, which cannot be returned in consecutive cycles due to lack of surface protection). Introducing the N-gpn@CC interlayer over the LPS@N-gpn cathode not only improved the capacity to 1153 mAh g^{-1} (3rd cycle)but also the cycle number to 100 cycles with a final capacity of 558 mAh g^{-1}. This indicates improved self discharge due to the polar interlayer, more dissolved polysulfide could be retained in the initial cycles and reactivated in the following, which results in improved performance.The initial low Coulombic efficiency of the interlayer cell might be due to the high porosity of interlayer may result shuttle effect. Inaddition, different sulfur loading 0.5, 0.75, 1, and 1.5 mg cm^{-2} were also tested with the same strategy (Fig. 2d). In this sequence, cells with lower sulfur loading had higher initial capacities, however, all cells showed degradation in capacity with cycle number. This is expected to be due to the trapping of irreversible crystalline polysulfide (discussed below). Corresponding coulombic efficiency plots of Fig. 2 (c, d) are shown in Fig. S5 (a, b). The rate studies of LPS@N-gpn, LPS@N-gpn interlayer cells are studied at various current densities (Fig. S6 a-c).

Furthermore, the redox voltages could also be identified by cyclic voltammetry (CV) measurements (Fig. 2e, f). The CV of the N-gpn@CC cell showed two cathodic peaks at 1.4 V and 1.0 V, which are nearly
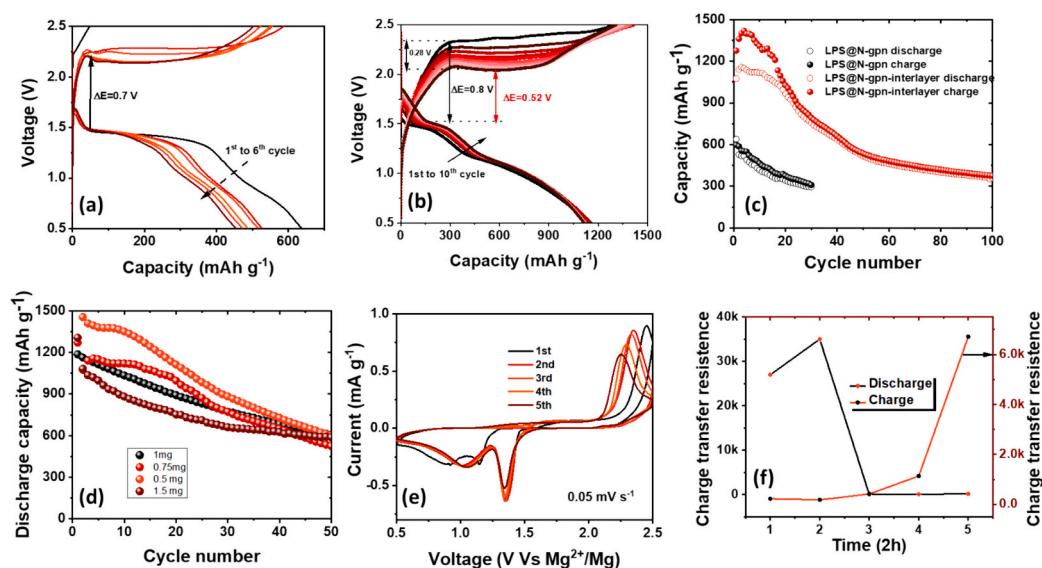

Fig. 2. Electrochemical studies. Charge-discharge profiles from galvanostatic cycling of cells with (a) LPS@N-gpn cathode (b) N-gpn@CC interlayer containing cathode. (c) Comparison of the cycling stability of LPS@N-gpn and N-gpn@CC interlayer containing cathode cells. (d) Cycling stability of a N-gpn@CC interlayer containing cathode cells with different sulfur loading. (e) CV of a N-gpn@CC interlayer cell. (f) Charge transfer resistance of N-gpn@CC interlayer cell at different points of discharge and charge.

consistent with the two-step reduction process of sulfur to sulfide in Fig. 2b. Similarly, one anodic peak at 2.4 V represents sulfide-to-sulfur conversion. Interestingly, similar to the findings of Fig. 2b, the decrease in the polarization with cycle number is also visible in the CV measurements. However, with the increase in the scan cycle the 2.4 V peak shifts to lower voltage. Fig. 2f shows the charge transfer resistance of N-gpn@CC interlayer cell at different points of discharge and charge, corresponding impedance plots are shown in Fig. S7. The huge charge transfer resistance during charging is due to the thick solid electrolyte interface (SEI) layer on Mg anode. After initial discharge, charge transfer resistance is decreased to three order of magnitude. However, the charge transfer resistance increased after charging due to the formation of nonconductive sulfur on the surface of the electrode.

2.3. In-situ XRD

Fig. 3a displays in-situ electrochemical X-ray diffraction patterns from the LPS@N-gpn cell measured at different voltage steps during the first galvanostatic discharge and charge cycle. At the OCV stage, the cathode shows amorphous nature. During initial discharge to 1.3 V, a new set of Bragg peaks is arising and these peaks intensify during complete discharge to 0.5 V. Interestingly, these new peaks do not match with elemental sulfur and MgS. We believed these are coming from solid magnesium polysulfides. Due to the absence of literature (JCPDS) XRD patterns of MgPS, we synthesized solid magnesium polysulfides on our own in the Ar atmosphere, the corresponding EDX measurements confirm an elemental composition of Mg: S of 2.07: 6.73 (Figs. S8–10), the electrolyte is also involved in crystal formation. In the next step, the synthesized MgPS was characterized with XRD, which evidenced the crystalline nature of the product (Fig. 3a, Mg_xS_y crystals). Furthermore, a good agreement was found between this pattern and the results for the cathode material of the discharged LPS@N-gpn cell, confirming the formation of crystalline magnesium polysulfides during the discharge of the cell. The absence of a feature from the complete discharge product (MgS) might indicate that the reaction is not completed at this voltage. During the charging process, the intensity of these solid Mg_xS_y peaks gradually decreased again, which specifies that the formation of these polysulfides is partially reversible during cycling. However, at the end of
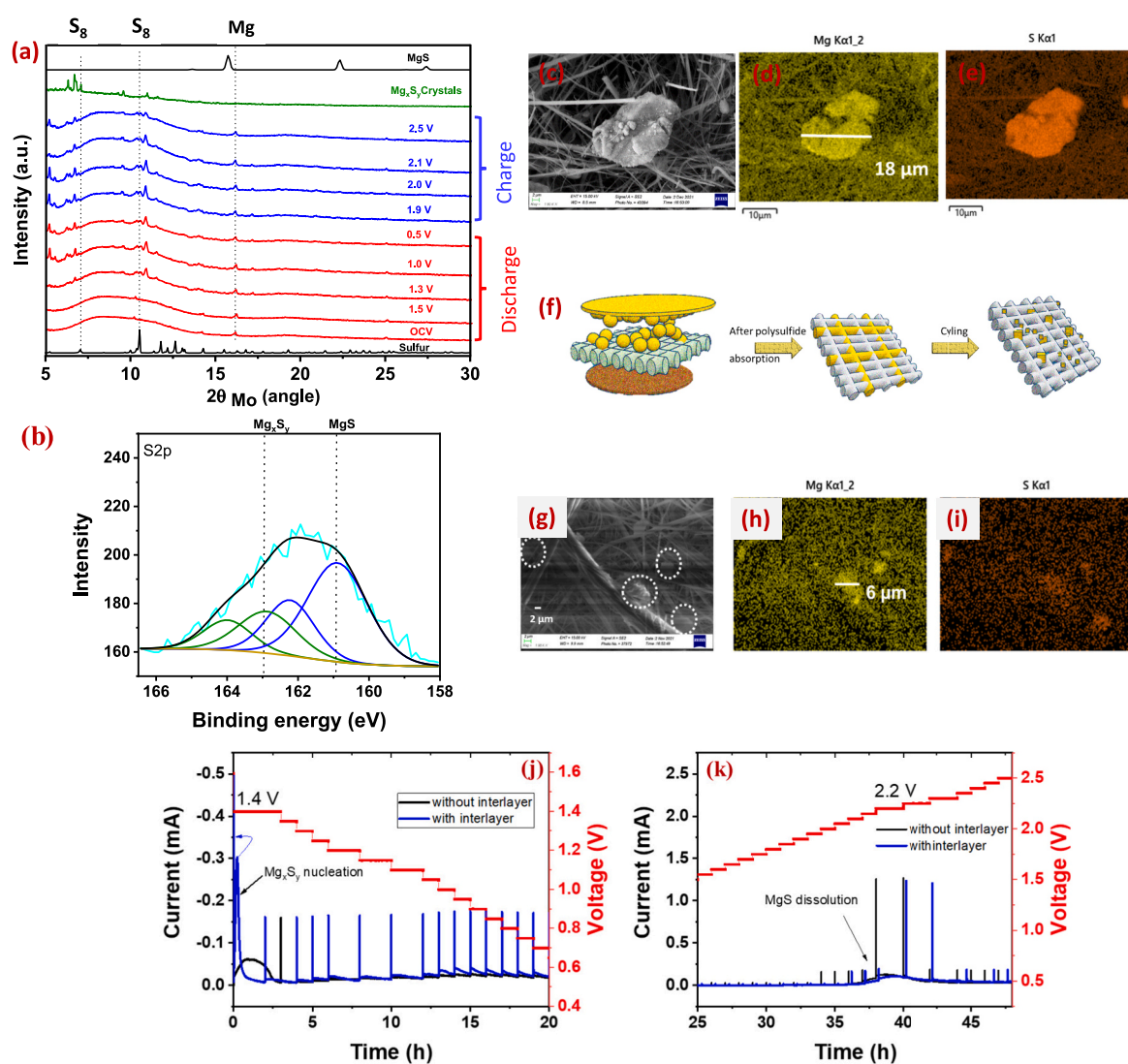

Fig. 3. (a) In-situ XRD measurements in an LPS@N-gpn cell. (b) XPS detail spectra in the S 2p region from a cycled separator of an LPS@N-gpn cell. (c-e) SEM and corresponding EDX elemental mapping results from a cycled separator of an LPS@N-gpn cell. (f) Schematic illustration of in-situ generated crystalline polysulfides on the separator in an Mg—S battery. Postmortem analysis of separator from N-gpn@CC cell after 100 cycles; (g) SEM image (circles indicates Mg_xS_y crystals) (h, i) corresponding EDX elemental mapping with Mg and S elements. Kinetic Evaluation of Polysulfide Conversion with and without interlayer. (j) PITT measurements of Mg|LPS@N-gpn cells with or without interlayer, the cells were discharged from 1.4 to 0.5 V with a step of 20 mV. (k) PITT measurements of Mg| LPS@N-gpn cells with or without interlayer, and the cells were charged from 1.6 to 2.5 V with a step of 20 mV.

charging (2.5 V), the polysulfides were not fully converted back to sulfur, and traces of these crystalline polysulfides could still be observed in the XRD pattern of the charged electrode.

It is important to mention that the measured in-situ XRD reflections are a combination of signals from the cathode and separator (the Mg anode was eliminated by keeping a hole in the center of Mg metal in the cell). Hence, to disentangle the different parts of the cell ex-situ experiments of cycled separator (Fig. 3b-e), cathode, and anode (Fig. 4) were carried out separately. For this purpose, the cell was dismantled inside the glove box for post-mortem analysis. The cycled electrodes and separator were recovered from the cell, washed with DME several times, and dried inside the glove box. Further, this separator was also analyzed by XPS and SEM to understand the structural and morphological changes of the separator during electrochemical cycling in more detail. Fig. 3b displays the XPS detail spectrum in the S 2p range of the cycled GFC separator, which confirms the presence of magnesium sulfide and magnesium polysulfide after cycling. Fig. 3 (c-e) shows the ex-situ SEM of a cycle separator. The separator contained solid particles with a diameter of around 18 μm, EDX elemental mapping of one of the particles confirms the existence of Mg and S. However, the amount of these polysulfides increases with cycling, and most of the time these solid particles are observed inside the separator (Fig. S11). Interestingly, solid particle formation was observed not only for the LPS@N-gpn cell (without interlayer) but also in the N-gpn@CC cell (with interlayer), but the size of the particles was much smaller in the latter case (with an average diameter of around 6 μm after 100 cycles) Fig. 3(g-i). This confirms the low Coulombic efficiency of interlayer cells in initial cycles. The slow crystallization process of Mg_xS_y on the separator is shown in Fig. 3f schematic.

To elucidate the impact of the interlayer on sulfur redox kinetics, potentiostatic intermittent titration technique (PITT) was employed to quantify the actual potential and capacity associated with MgS deposition and dissolution. PITT discharge profiles for the sulfur cathode typically exhibit two distinct regions (Fig. 3j). The first region corresponds to the liquid-to-solid conversion, where long-chain polysulfides are electrochemically reduced to short-chain solid polysulfides (Mg_xS_y). The second region signifies the solid-to-solid conversion, characterized by the deposition of MgS.

The pristine cathode displayed an immediate onset of the liquid-to-solid conversion at 1.4 V, manifested as a broad peak. Conversely, the interlayer cell exhibited a sharper peak, suggesting that the interlayer modifies the electrochemical equilibrium and accelerates the kinetics of this conversion process. The peak current for the cell without the interlayer reached 0.07 mA at 2.6 h, whereas the interlayer cell displayed a significantly higher peak current of 0.3 mA at only 0.5 h. This earlier peak time and higher peak current in the discharge PITT profile indicate faster kinetics for Mg_xS_y deposition in the presence of the interlayer. However, the interlayer cell exhibited a lower deposition capacity (113 mAh g^{-1} compared to 143 mAh g^{-1} for the cell without the interlayer) indicating lower amount of Mg_xS_y deposition.

Fig. 3k depicts the PITT curves for the charging process, which probes the dissolution of solid MgS. Fully discharged Mg | MgS cells were subjected to a potentiostatic charge for 1.0 h at the initial stage, followed by a series of potentiostatic charge steps of 1.0 h each, starting from 1.25 V with a voltage step size of 20 mV and maintained 2 h during phase transformation. The dissolution of MgS commenced at 2.20 V, as evidenced by prominent current peaks signifying the phase transition. Interestingly, the interlayer did not demonstrably influence the dissolution process, as evidenced by the comparable current responses and peak times observed for both cell configurations.

To further understand the impact of GFC separator on polysulfides and advantage of the interlayers, Mg—S cell is constructed by placing the interlayer between the separator and anode (separator ‖ anode) (Fig. S12). This configuration allows polysulfides directly on the separator, the corresponding cell shows significantly less initial capacity compared to the interlayer between the cathode and separator (cathode ‖ separator) cell and the capacity gradually drops with cycle number. This confirms that gradually dissolved polysulfides are trapped inside
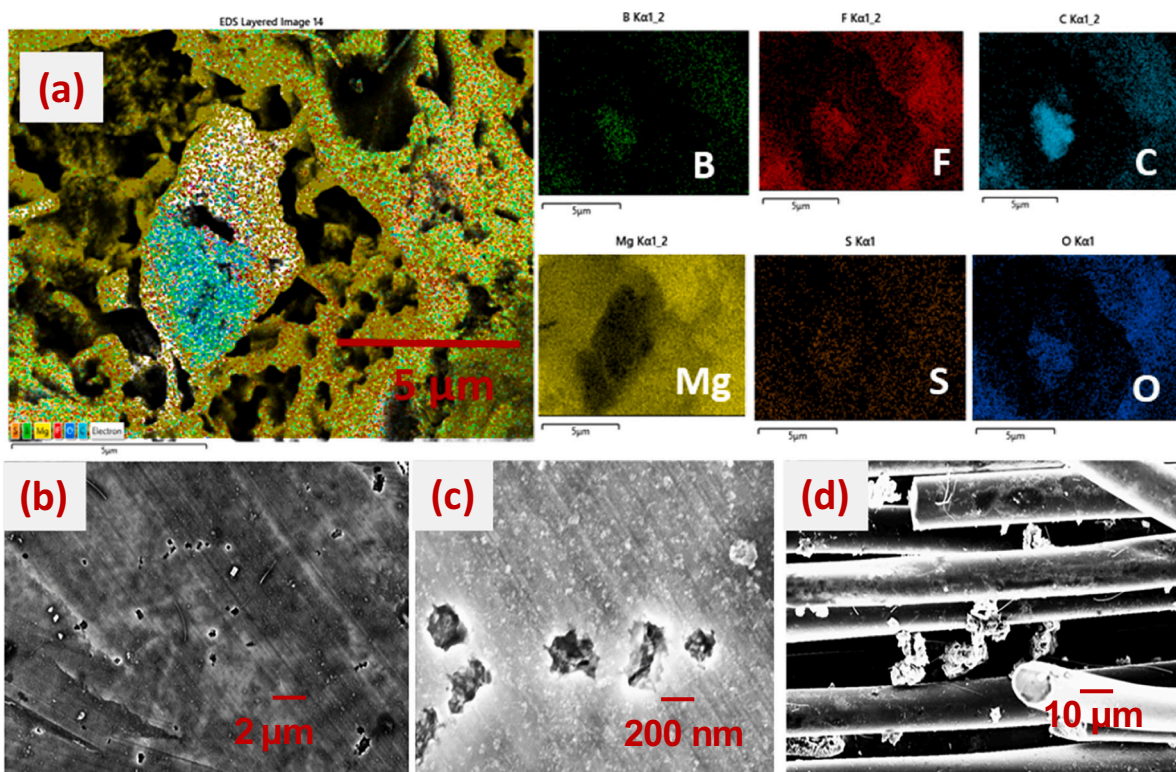

Fig. 4. (a) EDX elemental mapping of Mg anode from LPS@N-gpn cell after 30 cycles. (b, c) SEM images of Mg anodes with N-gpn@CC interlayer (d) cycled interlayer on Mg side with Mg trapping.

the separator and become crystalized and further not accessible due to the non-conductive nature of the separator. Interestingly, the cell cycle life of the battery increased to 300 cycles (Fig. 4b). This high cycle life is believed to be the protection of the Mg anode from polysulfide attack, which is not observed in LPS@N-gpn cells. The postmortem analysis of LPS@N-gpn and interlayer between the separator ‖ anode cell are shown in Fig. 4a-d. The elemental mapping (Fig. 4) of Mg metal in the LPS@N-gpn cell provides evidence of a significant amount of Mg loss, with the surface being composed of electrolyte and magnesium polysulfides. However, this undesirable scenario is mitigated with the protective measures in place.

To shed light on the experimental findings of improved polysulfide activity with N-gpn interlayer, we calculated the interaction energies of magnesium polysulfides with the N-gpn surface, as listed in Table 1. The corresponding adsorption configurations are illustrated in Fig. 5. MgS_8 adsorbs N-gpn (Fig. 5b), with a binding energy of -1.1 eV. Other polyanions such as MgS, MgS_4, and MgS_6 exhibit slightly lower (weaker) interaction energies than MgS_8 species, (Fig. S13). The positive interaction energy of MgS_2 indicates an unstable adsorption configuration. Interestingly, even for the S_8 polyanion (Fig. 5a), the adsorption energy is about -0.8 eV, showing a weaker interaction with the N-gpn surface than MgS_8. As shown in Fig. 5b, in the most favorable adsorption configuration of MgS_8 the magnesium atom does not become part of the S_8 polyanion chain but rather divides it into two parts, binding in total to four S atoms. Furthermore, despite its high coordination, the Mg atom still favorably absorbs on the N site of N-gpn. After describing the adsorption on N-gpn, we address the interaction of MgS_8 with the N-gpn with a carbon vacancy, denoted as the defective N-gpn. As shown in Fig. 5c, the magnesium atom of the MgS_8 is located almost directly above the defect center, making a bond with the nitrogen atom. The calculated interaction energy of MgS_8@ defective N-gpn is -1.58 eV, suggesting that the graphitic N located at a carbon vacancy is a favorable site for MgS_8 adsorption resulting in a stronger adsorption bond than other N-doping structures.

To gain additional insights into the chemistry of the S_8 and MgS_8 interaction with N-gpn and defective N-gpn, Fig. 5d, e displays the charge density difference, $\Delta\rho(r)$, for MgS_8@ N-gpn and MgS_8@defective N-gpn, respectively. In the $\Delta\rho(r)$ plots, the blue color represents electron charge accumulation, and the magenta color represents electron deficit regions upon the interaction of the species with the respective surfaces. The formation of Mg—N bonds is reflected by the blue-colored charge accumulation lobes close to the N atom in the MgS_8@defective N-gpn structure. These electron charge accumulation lobes are weaker for MgS_8@N-gpn compared to the defective structure, indicative of the relatively weak interaction of the single N atom with Mg adsorbed at the N-gpn surface. For S_8@N-gpn, no significant changes in the charge density upon adsorption have been found, indicating a negligible chemical interaction. This means that the interaction energy of 0.80 eV mainly originates from the dispersion interaction between the molecule and the surface.

2.4. Ex-situ XPS

The chemical state of sulfur on the LPS@N-gpn cathode and Mg

anode was investigated by XPS analysis at different stages of electrochemical cycling. Fig. 6 shows the results for discharged and charged samples in the 5th cycle, a pristine LPS@N-gpn sample was also carried out for comparison. Pristine LPS@N-gpn sample survey spectrum and high resolution N1s spectra are plotted in Fig. S14. The S2p detail spectrum of the pristine sample (Fig. 6a) shows two main peak doublets with the $S2p_{3/2}$ peaks at 162.4 and 163.9 eV (all binding energies in the following are for the $S2p_{3/2}$ peak), which indicates the presence of bridging (S_B) and terminal (S_T) sulfur atoms of polysulfide chains in the sample. In addition, another peak doublet at 169 eV appears at higher binding energy, which can be assigned to some oxidized S species (like sulfates). The spectrum of the discharge sample in Fig. 6b displays a different chemical state with sulfur in different oxidation states. Most prominently, another peak doublet due to MgS appears at lower binding energy (161.0 eV) in addition to the signals due to bridging and terminal S in polysulfides (Mg_xS_y). The persistence of the latter indicates that the reduction of MgS was not complete even in the 5th cycle discharge process. Fig. 6c shows the spectrum of the charged cathode. Essentially, a shift back to higher binding energies is observed, which indicates the transformation to elemental sulfur (164.0 eV) and polysulfides (162.5 eV), this demonstrates that complete conversion of MgS to S_8 is not observed during the charging. Taken together, the XPS analysis of these sulfur cathodes reflects the persistence of unreacted polysulfides inside the electrode during cycling.

Fig. 6 (d, e) displays the deconvoluted XPS spectra of the magnesium anode in the 5th cycle discharged and charged state. Both spectra reveal the presence of sulfide species on the surface, peak doublets due to MgS (161.0 eV) and polysulfides (162.6 eV) can be discerned, while the feature due to terminal S of polysulfides is absent [34,35]. This result confirms the operation of a polysulfide shuttle from cathode to anode leading to the accumulation of sulfide deposits on the anode surface during the cycling process, which may passivate the Mg anode during consecutive cycles. This might be one of the reasons for the continuous capacity fading observed in electrochemical cycling.

The cycled Mg anode of an LPS@N-gpn was also investigated by SEM and EDX mapping, main results are shown in Fig. S15. From the results, it becomes clear that the Mg anode of such a cell suffers from deterioration during cycling. Furthermore, elements B, F, and S are detected on the deteriorated anode surface. This indicates that the electrolyte, including polysulfides, was involved in anode deterioration. For comparison, the SEM images (Fig. S15) of the interlayer-protected Mg anode cell showed much less deterioration indicating a reduction of detrimental effects due to exposure of Mg to electrolytes and polysulfides.

3. Discussion

It was reported before that the rate of polysulfide dissolution in Mg—S batteries is considerably higher than in Li—S batteries and this might be a major issue for the cycling stability [36]. Here, we noticed in in-situ XRD (Fig. 5a) experiments that these dissolved polysulfides are converting to a crystalline solid inside the battery, the ex-situ XPS (Fig. 6) and SEM results (Fig. 5c, S10) indicate the formation of solid Mg_xS_y on the cathode (XRD, XPS), anode (XPS), and separator (XRD, SEM). The formation of this solid Mg_xS_y might take place during the discharge process by polysulfide dissolution and migration from the cathode to the separator. The borosilicate glass fiber (GFC) separator chemically/physically interacts/absorbs the liquid polysulfides and the absorbed material might transform over time into a solid due to the metastable nature of the liquid. The size of this solid particle depends on the cycle number. Most importantly, the solid particles are completely electrochemically inactive if they are trapped in/at the separator, and even in/at the cathode they are not completely active due to the poor conductivity (Fig. 5a, Fig. 6c). The continuous loss of active material from the cathode and precipitation on the separator might be the reason for the gradual capacity degradation. We also conducted tests with multiple GFC separators which brings down the cycle life of the cell
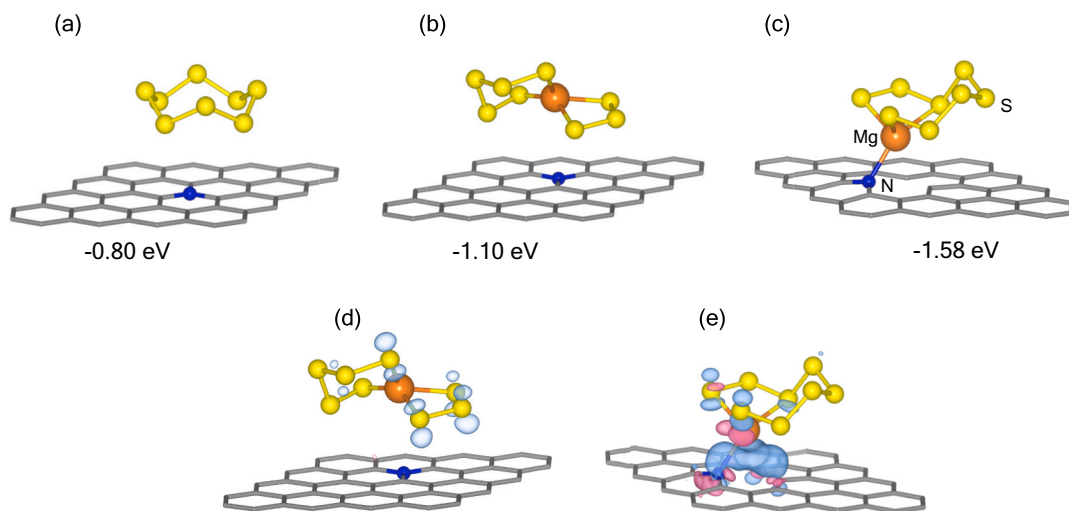
Table 1
The calculated interaction energies for MgS_n ($n = 1, 2, 4, 6, 8$) and S_8 species on N-gpn.

Species	Interaction energy (eV)
MgS@ N-gpn	-0.75
MgS_2@ N-gpn	0.19
MgS_4@ N-gpn	-0.60
MgS_6@ N-gpn	-0.72
MgS_8@ N-gpn	-1.10
MgS_8@defective N-gpn	-1.58
S_8@ N-gpn	-0.80

Fig. 5. Structural representations and calculated interaction energies of the investigated (a) S_8 and (b) MgS_8 species absorbed on N-gpn and (c) defective N-gpn. Blue spheres represent nitrogen atoms, yellow spheres represent sulfur, and orange ones show the magnesium cations. Gray hexagons represent the honeycomb lattice of graphene. The charge density differences are shown in (d), and (e) for the MgS_8 species adsorption on N-gpn and defective N-gpn respectively. (For interpretation of the references to color in this figure legend, the reader is referred to the web version of this article.)
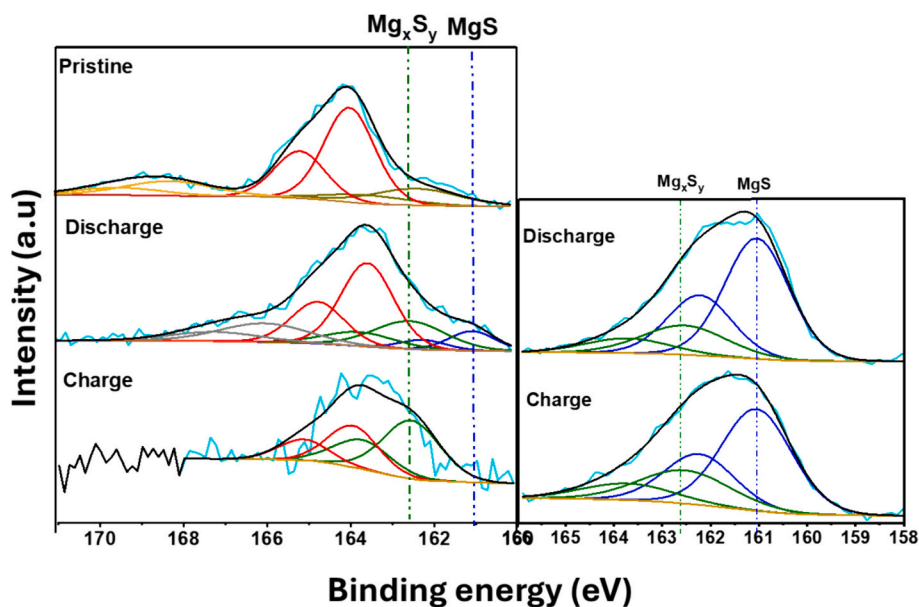

Fig. 6. XPS detail spectra in the S2p region of (a) pristine (b) discharged and (c) charged LPS@N-gpn cathode, and (d) discharged and (e) charged Mg anode. The cycled Mg anodes were recovered in the 5th electrochemical cycle.

quickly. Further, by inserting an interlayer between the cathode and separator (N-gpn@CC cell) the shuttling of dissolved polysulfide is significantly reduced; the polysulfides are trapped in the conductive interlayer during discharge and, due to the conductive nature, can be reactivated and utilized again during charging. As a result, this type of cell has higher capacity and better cycling stability. However, the porous nature of the interlayer still allows a part of the polysulfides to pass to the separator during cycling and become inactive there, this may cause the slow capacity fade and crystalline polysulfides are also observed for the N-gpn@CC cell. However, this cathode protection process increases cycling stability to 100 cycles but a similar protection strategy on Mg anode improves cycling stability to 300 cycles.

4. Conclusions

In the present work, we noticed in addition to polysulfide shuttling that large amounts of active material are trapped inside the separator which could limit Mg—S battery cyclability. Overall, the in-situ and ex-situ results confirm the formation of intermediate crystalline polysulfides in addition to MgS in the Mg—S battery. Unlike lithium polysulfides in a Li—S battery, these polysulfides are metastable in the electrolyte and precipitate as solid over the cathode, separator, and anode. Our calculations identify the stronger interactions of MgS_8 with N-gpn compared to other polysulfides, as well as the formation of Mg—N bonds in the interaction of MgS_8 and defective N-gpn. Therefore, the defective N-gpn provides more reactive anchoring points, trapping the magnesium polysulfides. Further, the active material trapped inside the separator and the Mg anode corrosion are also noticed during cycling.

Hence, these are the major reasons for capacity degradation and limited cyclability in Mg—S batteries. A modified cell configuration (N-gpn@CC) with an interlayer between the cathode and separator turned out to improve cyclability considerably by reducing the polysulfide shuttle. The cell capacity significantly improved after using interlayer from 638 mAh g^{-1} to 1075 mAh g^{-1} and the cell maintained a capacity of after 100 cycles. However, by protecting the anode the cyclability is further increased to 300 cycles. This emphasizes that Mg anode protection is much more important in Mg—S batteries.

5. Experimental section

5.1. Material preparation

Electrolyte preparation: Magnesium hexafluoroisopropyl borate salt (Mg[B(hfip)$_4$]$_2$) was synthesized according to our previous reports [37], and 0.4 M Mg[B(hfip)$_4$]$_2$ electrolyte was prepared in dimethoxyethane (DME) (dried for 3 days in 3–4 Å molecular sieves) solvent and used as the chloride-free electrolyte.

Catholyte synthesis: Li$_2$S powder and sublimed elemental sulfur powder (S$_8$) were added to the blank electrolyte in a ratio of 3:4 (3 S$_8$ + 4 Li$_2$S → 4 Li$_2$S$_6$) to obtain a 0.1 M LPS. This solution was prepared in an argon-filled glove box (H$_2$O < 0.1 ppm, O$_2$ < 0.1 ppm) and stirred overnight at 50 °C. Further, this solution was left for a week, to allow a complete reaction. The conversion of the solution from colorless to red-brown solution indicates polysulfide formation.

Synthesis of electrode: At first, 10 wt% PVP was dissolved in water, then 90 wt% N-gpn was added, and the composite solution was stirred overnight. This slurry was cast on carbon-coated Al foil and also on activated carbon cloth, labeled as N-gpn and N-gpn@CC. The electrodes are dried overnight in a vacuum oven at 70 °C. Further, N-gpn@CC was used as an interlayer. The thickness of the interlayer: 270 μm, Areal mass loading: 9.7 mg cm^{-2}.

Cell fabrication: The 2032-type coin cells were assembled inside the glovebox (MBRAUN, H$_2$O < 0.1 ppm, O$_2$ < 0.1 ppm). The 1 mg containing liquid polysulfides (LPS) was placed above the N-gpn coated Al electrode (LPS@N-gpn) and used as a cathode. In the case of interlayer cells, N-gpn@CC interlayer was placed above this cathode. Further, two glass fiber filter papers (GF/C Whatman) were employed over the interlayer and soaked with 100 μL of 0.4 M Mg[B(hfip)$_4$]$_2$/DME electrolyte, polished Mg foil was used as anode (the oxide layer on Mg foil was scratched with the help of a knife inside the glovebox). The active material loading on each cell was limited to 1 mg cm^{-2}.

CRediT authorship contribution statement

Dasari Bosubabu: Writing – original draft, Validation, Methodology, Formal analysis, Data curation, Conceptualization. **Mohsen Sotoudeh:** Writing – original draft, Visualization, Software, Formal analysis, Conceptualization. **Liping Wang:** Writing – review & editing, Visualization, Methodology, Formal analysis, Conceptualization. **Zhenyou Li:** Writing – review & editing, Conceptualization. **Thomas Diemant:** Writing – review & editing, Writing – original draft, Methodology. **Guruprakash Karkera:** Writing – review & editing, Methodology, Conceptualization. **Ebrahim Abouzari-Lotf:** Writing – review & editing, Data curation. **Axel Groß:** Writing – review & editing, Supervision, Data curation. **Maximilian Fichtner:** Writing – review & editing, Supervision, Project administration, Investigation, Funding acquisition. **Zhirong Zhao-Karger:** Writing – review & editing, Supervision, Project administration, Funding acquisition.

Declaration of competing interest

The authors declare the following financial interests/personal relationships which may be considered as potential competing interests: Dasari Bosubabu reports financial support was provided by Federal Ministry of Education and Research (Bundesministerium für Bildung und Forschung, BMBF) of Germany. If there are other authors, they declare that they have no known competing financial interests or personal relationships that could have appeared to influence the work reported in this paper.

Data availability

Data will be made available on request.

Appendix A. Supplementary data

Structural Characterization, Electrochemical Characterization, rate studies, impedance plots, Mg protection and its cycling stability, and details of the Electronic Structure Calculation. Supplementary data to this article can be found online at https://doi.org/10.1016/j.est.2024.113389.

References

[1] A. Manthiram, A reflection on lithium-ion battery cathode chemistry, Nat. Commun. 11 (2020) 1–9, https://doi.org/10.1038/s41467-020-15355-0.
[2] N. Nitta, F. Wu, J.T. Lee, G. Yushin, Li-ion battery materials: present and future, Mater. Today 18 (2015) 252–264, https://doi.org/10.1016/j.mattod.2014.10.040.
[3] L. Wang, Z. Li, Z. Meng, Y. Xiu, B. Dasari, Z. Zhao-Karger, M. Fichtner, Designing gel polymer electrolyte with synergetic properties for rechargeable magnesium batteries, Energy Storage Materials 48 (2022) 155–163, https://doi.org/10.1016/j.ensm.2022.03.006.
[4] Z. Zhao-Karger, X. Zhao, D. Wang, T. Diemant, R.J. Behm, M. Fichtner, Performance improvement of magnesium sulfur batteries with modified non-nucleophilic electrolytes, Adv. Energy Mater. 5 (2015) 1401155, https://doi.org/10.1002/aenm.201401155.
[5] M. Rashad, M. Asif, Z. Ali, Quest for magnesium-sulfur batteries: current challenges in electrolytes and cathode materials developments, Coord. Chem. Rev. 415 (2020) 213312, https://doi.org/10.1016/j.ccr.2020.213312.
[6] Z. Zhao-Karger, M. Fichtner, Magnesium-sulfur battery: its beginning and recent progress, MRS Communications 7 (2017) 770–784, https://doi.org/10.1557/mrc.2017.101.
[7] Z. Zhao-Karger, M. Fichtner, Beyond intercalation chemistry for rechargeable Mg batteries: a short review and perspective, Front. Chem. 7 (2019) 1–12, https://doi.org/10.3389/fchem.2018.00656.
[8] Z. Ma, D.R. MacFarlane, M. Kar, Mg cathode materials and electrolytes for rechargeable Mg batteries: a review, Batteries and Supercaps 2 (2019) 115–127, https://doi.org/10.1002/batt.201800102.
[9] M.S. Ding, T. Diemant, R.J. Behm, S. Passerini, G.A. Giffin, Dendrite growth in mg metal cells containing Mg(TFSI) 2 /Glyme electrolytes, J. Electrochem. Soc. 165 (2018) A1983–A1990, https://doi.org/10.1149/2.1471809jes.
[10] S. Dongmo, S. Zaubitzer, P. Schüler, S. Krieck, L. Jörissen, M. Wohlfahrt-Mehrens, M. Westerhausen, M. Marinaro, Stripping and plating a magnesium metal anode in bromide-based non-nucleophilic electrolytes, ChemSusChem 13 (2020) 3530–3538, https://doi.org/10.1002/cssc.202000249.
[11] L. Yang, Q. Li, Y. Wang, Y. Chen, X. Guo, Z. Wu, G. Chen, B. Zhong, W. Xiang, Y. Zhong, A review of cathode materials in lithium-sulfur batteries, Ionics 26 (2020) 5299–5318, https://doi.org/10.1007/s11581-020-03767-3.
[12] Y. Li, J.G. Shapter, H. Cheng, G. Xu, G. Gao, Recent progress in sulfur cathodes for application to lithium–sulfur batteries, Particuology 58 (2021) 1–15, https://doi.org/10.1016/j.partic.2021.01.008.
[13] M. Zhao, B.Q. Li, X.Q. Zhang, J.Q. Huang, Q. Zhang, A perspective toward practical lithium-sulfur batteries, ACS Cent. Sci. 6 (2020) 1095–1104, https://doi.org/10.1021/acscentsci.0c00449.
[14] Z. Li, X. Mu, Z. Zhao-Karger, T. Diemant, R.J. Behm, C. Kübel, M. Fichtner, Fast kinetics of multivalent intercalation chemistry enabled by solvated magnesium-ions into self-established metallic layered materials, Nat. Commun. 9 (2018) 1–13, https://doi.org/10.1038/s41467-018-07484-4.
[15] M. Rashad, H. Zhang, X. Li, H. Zhang, Fast kinetics of Mg2+/Li+ hybrid ions in a polyanion Li3V2(PO4)3 cathode in a wide temperature range, J. Mater. Chem. A 7 (2019) 9968–9976, https://doi.org/10.1039/c9ta00502a.

[16] A. Gross, M. Fichtner, Insights into the electrochemical processes of rechargeable magnesium – sulfur batteries with a new cathode design †, 2019, pp. 25490–25502, https://doi.org/10.1039/c9ta09155f.

[17] R. Mohtadi, O. Tutusaus, T.S. Arthur, Z. Zhao-Karger, M. Fichtner, The metamorphosis of rechargeable magnesium batteries, Joule 5 (2021) 581–617, https://doi.org/10.1016/j.joule.2020.12.021.

[18] B.P. Vinayan, Z. Zhao-Karger, T. Diemant, V.S.K. Chakravadhanula, N. I. Schwarzburger, M.A. Cambaz, R.J. Behm, C. Kübel, M. Fichtner, Performance study of magnesium-sulfur battery using a graphene based sulfur composite cathode electrode and a non-nucleophilic Mg electrolyte, Nanoscale 8 (2016) 3296–3306, https://doi.org/10.1039/c5nr04383b.

[19] D. Bosubabu, S. Ramakumar, S. Jeevanantham, I. Kanagaraj, P.B. Bhargav, N. Ahmed, K. Ramesha, In-situ Lithiated SiO2 as Lithium-free anode for lithium-sulfur batteries, Batteries and Supercaps 5 (2022) e202200262, https://doi.org/10.1002/batt.202200262.

[20] D.B. Babu, K. Giribabu, K. Ramesha, Permselective SPEEK/Nafion composite-coated separator as a potential polysulfide crossover barrier layer for Li-S batteries, ACS Appl. Mater. Interfaces 10 (2018) 19721–19729, https://doi.org/10.1021/acsami.8b04888.

[21] L. Wang, P. Jankowski, C. Njel, W. Bauer, Z. Li, Z. Meng, B. Dasari, T. Vegge, J.M. G. Lastra, Z. Zhao-Karger, M. Fichtner, Dual role of Mo6S8 in polysulfide conversion and shuttle for Mg–S batteries, Adv. Sci. 9 (2022) 1–9, https://doi.org/10.1002/advs.202104605.

[22] L. Chen, H. Yu, W. Li, M. Dirican, Y. Liu, X. Zhang, Interlayer design based on carbon materials for lithium-sulfur batteries: a review, J. Mater. Chem. A 8 (2020) 10709–10735, https://doi.org/10.1039/d0ta03028g.

[23] D.B. Babu, K. Ramesha, Melamine assisted liquid exfoliation approach for the synthesis of nitrogen doped graphene-like carbon nano sheets from bio-waste bagasse material and its application towards high areal density Li-S batteries, Carbon 144 (2019) 582–590, https://doi.org/10.1016/j.carbon.2018.12.101.

[24] Y. Liu, H. Wei, X. Zhai, F. Wang, X. Ren, Y. Xiong, O. Akiyoshi, K. Pan, F. Ren, S. Wei, Graphene-based interlayer for high-performance lithium–sulfur batteries: a review, Mater. Des. 211 (2021) 110171, https://doi.org/10.1016/j.matdes.2021.110171.

[25] L. Wang, Z. Yang, H. Nie, C. Gu, W. Hua, X. Xu, X. Chen, Y. Chen, S. Huang, A lightweight multifunctional interlayer of sulfur-nitrogen dual-doped graphene for ultrafast, long-life lithium-sulfur batteries, J. Mater. Chem. A 4 (2016) 15343–15352, https://doi.org/10.1039/c6ta07027b.

[26] H. Deng, L. Yao, Q.A. Huang, Q. Su, J. Zhang, G. Du, Highly improved electrochemical performance of Li-S batteries with heavily nitrogen-doped three-dimensional porous graphene interlayers, Mater. Res. Bull. 84 (2016) 218–224, https://doi.org/10.1016/j.materresbull.2016.08.014.

[27] J. Tian, F. Xing, Q. Gao, Graphene-based nanomaterials as the cathode for lithium-sulfur batteries, Molecules 26 (2021) 1–28, https://doi.org/10.3390/molecules26092507.

[28] S. Li, T. Mou, G. Ren, J. Warzywoda, B. Wang, Z. Fan, Confining sulfur species in cathodes of lithium-sulfur batteries: insight into nonpolar and polar matrix surfaces, ACS Energy Lett. 1 (2016) 481–489, https://doi.org/10.1021/acsenergylett.6b00182.

[29] D.B. Babu, K. Ramesha, Constraining polyselenide formation in ether based electrolytes through confinement of Se in microporous carbon matrix for Li-Se batteries, Electrochim. Acta 219 (2016) 295–304, https://doi.org/10.1016/j.electacta.2016.10.026.

[30] D. Bosubabu, R. Sampathkumar, G. Karkera, K. Ramesha, Facile approach to prepare multiple heteroatom-doped carbon material from bagasse and its applications toward lithium-ion and lithium−sulfur batteries, Energy and Fuels 35 (2021) 8286–8294, https://doi.org/10.1021/acs.energyfuels.0c03887.

[31] D. Bosubabu, J. Sivaraj, P. Gurunathan, K. Ramesha, Hollow Co3O4 microspheres grafted with nitrogen-doped carbon nanotubes as efficient sulfur host for high performing lithium-sulfur batteries, Energy Fuels 34 (2020) 16810–16818, https://doi.org/10.1021/acs.energyfuels.0c03104.

[32] D. Bosubabu, V. Parthiban, A.K. Sahu, K. Ramesha, Nitrogen-doped graphene-like carbon from bio-waste as efficient low-cost electrocatalyst for fuel cell application, Bull. Mater. Sci. 44 (2021), https://doi.org/10.1007/s12034-021-02367-9.

[33] D. Bosubabu, Z. Li, Z. Meng, L.P. Wang, M. Fichtner, Z. Zhao-Karger, Mitigating self-discharge and improving the performance of Mg-S battery in Mg[B(hfip)4] 2electrolyte with a protective interlayer, J. Mater. Chem. A 9 (2021) 25150–25159, https://doi.org/10.1039/d1ta06114c.

[34] M. Fantauzzi, B. Elsener, D. Atzei, A. Rigoldi, A. Rossi, Exploiting XPS for the identification of sulfides and polysulfides, RSC Adv. 5 (2015) 75953–75963.

[35] X. Liang, C. Hart, Q. Pang, A. Garsuch, T. Weiss, L.F. Nazar, A highly efficient polysulfide mediator for lithium–sulfur batteries, Nature com. 6 (5682) (2015) 1–8.

[36] R. Richter, J. Häcker, Z. Zhao-Karger, T. Danner, N. Wagner, M. Fichtner, K. A. Friedrich, A. Latz, Insights into self-discharge of lithium- and magnesium-sulfur batteries, ACS Applied Energy Materials 3 (2020) 8457–8474, https://doi.org/10.1021/acsaem.0c01114.

[37] Z. Zhao-Karger, R. Liu, W. Dai, Z. Li, T. Diemant, B.P. Vinayan, C. Bonatto Minella, X. Yu, A. Manthiram, R.J. Behm, M. Ruben, M. Fichtner, Toward highly reversible magnesium-sulfur batteries with efficient and practical Mg[B(hfip)4]2 electrolyte, ACS Energy Letters 3 (2018) 2005–2013, https://doi.org/10.1021/acsenergylett.8b01061.